Hindawi Publishing Corporation
Journal of Spectroscopy
Volume 2015, Article ID 541958, 12 pages
http://dx.doi.org/10.1155/2015/541958

Research Article

$SrAl_2O_4$:Eu^{2+}(,Dy^{3+}) Nanosized Particles: Synthesis and Interpretation of Temperature-Dependent Optical Properties

Huayna Terraschke,[1] Markus Suta,[1] Matthias Adlung,[1] Samira Mammadova,[2] Nahida Musayeva,[2] Rasim Jabbarov,[2] Mihail Nazarov,[3] and Claudia Wickleder[1]

[1]*Inorganic Chemistry, Department of Science and Engineering, University of Siegen, Adolf-Reichwein Street 2, 57068 Siegen, Germany*
[2]*Institute of Physics, Azerbaijan National Academy of Sciences, G. Javid Avenue 33, 1143 Baku, Azerbaijan*
[3]*Institute of Applied Physics, Academy Sciences of Moldova, Academiei Street 5, 2028 Chisinau, Moldova*

Correspondence should be addressed to Claudia Wickleder; wickleder@chemie.uni-siegen.de

Received 9 November 2014; Accepted 17 January 2015

Academic Editor: Masaki Oura

$SrAl_2O_4$ nanosized particles (NPs) undoped as well as doped with Eu^{2+} and Dy^{3+} were prepared by combustion synthesis for the discussion of their intensively debated spectroscopic properties. Emission spectra of $SrAl_2O_4$:Eu^{2+}(,Dy^{3+}) NPs are composed by a green band at 19 230 cm^{-1} (520 nm) at room temperature, assigned to anomalous luminescence originated by Eu^{2+} in this host lattice. At low temperatures, a blue emission band at 22 520 cm^{-1} (444 nm) is observed. Contrary to most of the interpretations provided in the literature, we assign this blue emission band very reliably to a normal $4f^6(^7F_J)5d(t_{2g}) \rightarrow 4f^7(^8S_{7/2})$ transition of Eu^{2+} substituting the Sr^{2+} sites. This can be justified by the presence of a fine structure in the excitation spectra due to the different ^7F_J levels ($J = 0 \cdots 6$) of the $4f^6$ core. Moreover, Fano antiresonances with the ^6I_J ($J = 9/2, 7/2$) levels could be observed. In addition, the Stokes shifts (ΔE_S = 1 980 cm^{-1} and 5 270 cm^{-1} for the blue and green emission, resp.), the Huang-Rhys parameters of $S = 2.5$ and 6, and the average phonon energies of $\hbar\omega$ = 480 cm^{-1} and 470 cm^{-1} coupled with the electronic states could be reliably determined.

1. Introduction

Oxide-based inorganic phosphors doped with divalent europium are extremely advantageous due to their high brightness, enhanced chemical and thermal stabilities, and tunable emission wavelength from UV to red and low toxicity. Therefore, these phosphors are important for technological and industrial applications such as the production of fluorescent lamps, light emitting diodes (LEDs), or emissive displays for computers and mobile telephones [1, 2]. In general, Eu^{2+}-based phosphors are characterized by rather broad emission bands upon excitation, caused by the parity-allowed electronic transition from the lowest $4f^65d^1$ excited state into the $4f^7$ ground state. The emission wavelength is related to the position of this state with respect to the $4f^7$ ground state and is strongly influenced by the host lattice [3]. Within the host lattice, the decisive influence parameters are: (i) the coordination number of the cationic sites to be occupied by Eu^{2+}, (ii) the nephelauxetic effect, which is caused by the covalence, and (iii) the bond length between cations and ligands. In strontium aluminate lattices, for instance, Eu^{2+} ions emit radiation at 19 310 cm^{-1} (518 nm) in the case of $SrAl_2O_4$:Eu^{2+} and at 20 450 cm^{-1} (489 nm) for $Sr_4Al_{14}O_{25}$:Eu^{2+}, respectively [4–7].

Long afterglow bulk materials such as $SrAl_2O_4$:Eu^{2+},Dy^{3+} were discovered in 1996 by Matsuzawa et al. [7] and have been intensively investigated until today. Although the reduction of the particle size up to the nanoscale improves the applicability of luminescent materials due to the consequent high packing density, low light scattering effects, and easy suspendability in liquid media, the optical properties of the nanosized particles described here are not changed compared to the respective bulk materials in contrast to quantum dots. Numerous applications for afterglow nanomaterials have been reported in the literature, for example, safety indicators on emergency devices, traffic signs, power-saving of light

sources, writing and printing inks, plasma display phosphors, and bioimaging [4–10]. For bioimaging, afterglow materials offer a solution for the autofluorescence problem, in which fluorescent materials existing in the living cells are excited in parallel with the marker [10]. For this reason, in the ideal case, the marker must emit light after the excitation light is blocked. An additional biomedical application is in light sources for photodynamic therapy (PDT), where afterglow light is applied to produce singlet oxygen for cancer cell destruction [10].

Theories for explaining the afterglow mechanism have been intensively discussed by, for example, Yang et al. [9], Hölsä and coworkers [11–14], and so forth. Typically, the afterglow process in a host lattice doped with divalent europium and codoped with a trivalent lanthanide ion, for example, Dy^{3+}, is associated to the formation of an electron-and-hole trapping system. One of the theories, for instance, states that the afterglow effect results from the thermally activated release of a hole from Eu^{2+} in its excited state to the valence band, which is subsequently trapped by Dy^{3+}. The further thermally activated release of the hole from Dy^{4+} and recombination with Eu^{+} generate the persistent luminescence [7]. However, X-ray absorption near edge structure (XANES) spectroscopy did not detect the presence of Dy^{4+} and Eu^{+} in this system and the understanding of the afterglow principle is still considered open [11–14].

Besides the mechanism of the afterglow effect on $SrAl_2O_4$:Eu^{2+},Dy^{3+}, there is another spectroscopic behaviour of europium-doped strontium aluminate, which is still under intensive discussion. As explained before, the emission spectrum of $SrAl_2O_4$:Eu^{2+} at room temperature is characterized by a nearly Gaussian-shaped band centered at 19 310 cm^{-1}, assigned in the literature to the $4f^6 5d^1 \rightarrow 4f^7$ electronic transition of Eu^{2+} [3, 4]. In contrast, cooling Eu^{2+}-doped $SrAl_2O_4$ down to very low temperatures, for example, 10 K, causes a splitting of the emission spectrum into two bands. These two bands are centered at approximately 19 080 cm^{-1} and 22 520 cm^{-1} and have not been adequately explained until now [15–23].

Combustion synthesis, also called modified solid-state reaction, is applied for the preparation of highly crystalline compounds, for example, complex oxides such as aluminates [24], orthosilicates [25], and chromites [26] and has been successfully applied for the synthesis of $SrAl_2O_4$:Eu(,Dy) nanoparticles by several authors [24, 27–32]. The process consists of an exothermic redox reaction of an oxidizer, for example, metal nitrates and a reducing organic fuel, for example, urea [1]. Urea is reported to act additionally as a dispersive agent for the nanoparticles [33].

In the present work, $SrAl_2O_4$:Eu^{2+}(,Dy^{3+}) NPs were synthesized by means of combustion synthesis for the careful characterization and detailed interpretation of their still intensively debated optical properties. The obtained data was applied, for instance, for proposing a new model for understanding the origin of the low-temperature emission band at 22 520 cm^{-1} as well as for calculating the respective Stokes shift, Huang-Rhys parameter, and average phonon energy.

Table 1: Denomination and doping concentration of $SrAl_2O_4$ NPs.

Compound	Eu concentration/mol%	Dy concentration/mol%
1	0.0	0.0
2	0.1	0.0
3	0.5	0.0
4	1.0	0.0
5	1.0	2.0

2. Experimental Section

All reagents were commercially purchased and used without further purification. The applied method for the preparation of the strontium aluminate nanosized particles consists of an adaptation of the combustion synthesis suggested by Peng et al. [24]. For the spectroscopic investigations, $SrAl_2O_4$ nanosized particles with different doping concentrations were prepared, for which detailed information about denominations and compositions is presented on Table 1. For the investigation of the optical properties, samples without any doping, as well as with different Eu doping concentration and 1 mol% Eu and 2 mol% Dy, were prepared. However, for a detailed understanding, different Eu/Dy doping ratios have to be chosen, which will be the content of a future work.

For the synthesis, stoichiometric amounts of $Sr(NO_3)_2$ (Merck Chemicals, Darmstadt, Germany), $Al(NO_3)_3{\cdot}9H_2O$ (Merck Chemicals, 98.5%), $Eu(NO_3)_3{\cdot}6H_2O$ (Chempur, Karlsruhe, Germany, 99.9%), and $Dy(NO_3)_3{\cdot}5H_2O$ (Alfa Aesar, Karlsruhe, Germany, 99.9%) were dissolved in water together with the 20-fold molar excess of NH_2CONH_2 (Alfa Aesar, 99+%). The solution was placed in a preheated muffle furnace at 600°C. At this temperature, the solution evaporates, generating a large amount of gases, for example, oxides of carbon and nitrogen and also ammonia. Afterwards, the organic fuel causes the combustion, which releases the energy necessary for the reaction synthesis of the nanopowder. The complete reaction lasts about 5 to 10 minutes and the large amount of gases passes through the product, resulting in a very voluminous precursor [24, 33]. The gases also have a reductive character causing already the partial reduction from Eu^{3+} to Eu^{2+}. In the next step, the precursor was annealed at 1100°C for 1 h under an Ar/H_2 reductive atmosphere.

Photoluminescence measurements at room and low temperatures were performed with the aid of a Fluorolog3 spectrofluorometer Fl3-22 (Horiba Jobin Yvon, Longjumeau, France) equipped with double Czerny-Turner monochromators, a 450 W xenon lamp, and a R928P photomultiplier (Hamamatsu, Herrsching, Germany) with a photon counting system. Cooling down to 10 K was achieved by a closed-cycle He cryostat (Janis Research, Wilmington, United States). Measurements at high temperature (up to 500 K) were carried out a with a FluoroMax fluorescence spectrometer (Horiba Jobin Yvon, Longjumeau, France), also equipped with two monochromators and a 150 W xenon lamp, combined with an attached oven. The emission spectra were corrected for photomultiplier sensitivity, the excitation spectra for lamp intensity, and both for the transmission

of the monochromators. X-ray powder diffraction patterns were measured on a D5000 X-ray diffractometer (Siemens, Karlsruhe, Germany) operating at 40 kV, 30 mA. Particle size distribution was measured on a Zetasizer Nano S90 (Malvern Instruments, Herrenberg, Germany) at a 90° scattering angle using dynamic light scattering. Microscopic analysis was carried out on an atomic force microscope (AFM) Multimode 2, applying an AC200TS cantilever. Raman measurements were performed at room temperature by Raman Horiba Jobin Yvon HR800UV with excitation through a microscope using the 514.5 nm line of an Ar^+ laser, as well as by an inVia Raman Microscope (RENISHAW, Old Town, Wotton-under-Edge, Gloucestershire GL12 7DW, United Kingdom) using an excitation source of 633 nm by the combination of He and Ne sources with an exposure time of 20 s. Two lasers with 514.5 nm and 633 nm wavelengths were used. As the laser wavelength gets shorter, Raman scattering efficiency increases, but, at the same time, the risk of fluorescence also increases. Therefore, we used the 514.5-nm excitation to study only for the undoped host lattice of $SrAl_2O_4$ and 633 nm for the doped materials. The Raman spectrum was obtained in a spectral range of 100–1000 cm^{-1} using the 514.5 nm excitation wavelength from a continuous wave Ar^+ laser at room temperature. Incident light is focused on a sample through an optical microscope with a spatial resolution of $<2\,\mu$m in the backscattering geometry. The optical parameters of the sample were measured using an optical sphere (Everfine, Hangzhou, China) which was powered by the Everfine WY CC&CV DC power supply. The optical sphere was connected via optical fibre to the PMS-80 spectrophotocolorimeter (EVERFINE, Hangzhou, China), which is capable of measuring light within the UV and near IR spectra. The data was analyzed by PmsLab V3.00.123 software (EVERFINE, Hangzhou, China).

3. Results and Discussion

3.1. Size Analysis of $SrAl_2O_4$:Eu^{2+} and $SrAl_2O_4$:Eu^{2+}, Dy^{3+} NPs. Powder X-ray diffraction analysis of compounds **1–5** revealed the high crystallinity and purity of the strontium aluminate phase after the combustion synthesis and after the annealing process (Figure 1). The broadening and partial overlap of the reflections, for instance, at $2\theta = 34°$ and 35°, indicate the small size of the measured crystals.

Postannealing processes can cause the coalescence and the agglomeration of the NPs, playing a significant role on the particle size. As demonstrated by means of dynamic light scattering (DLS, Figure 2(a)), the size of the $SrAl_2O_4$:Eu NPs increased from 70–200 nm to 200–450 nm after sintering at 1100°C. Particles annealed at 1100°C were additionally characterized with aid of atomic force microscopy, as shown at Figure 3. Here, the particle size measured with aid of the cross section AFM analysis lies in the range of 200–300 nm. Dynamic light scattering measurements are important for acquiring information about the particle size distribution. However, the measurement is influenced by the formation of agglomerates, due to mutual attractive interactions between nanoparticles, accentuated in liquid media. The formation of agglomerates may explain the minor deviation between the AFM and the DLS measurements. Even though the DLS analysis revealed the formation of small agglomerates, the $SrAl_2O_4$:Eu^{2+} NPs are able to form stable suspensions in liquid media, for example, ethanol that shows bright green luminescence under UV light (Figure 2(b)).

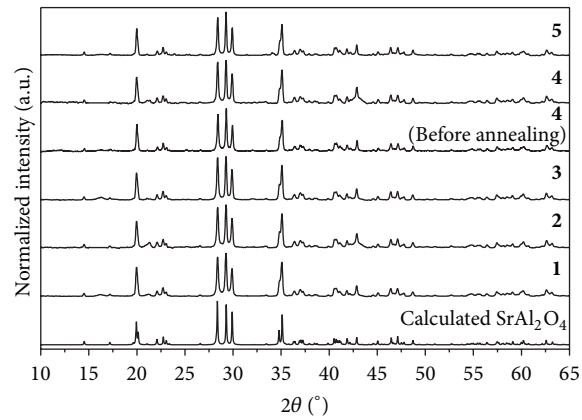

Figure 1: X-ray diffraction analysis of compounds **1–5** in comparison to the calculated diffraction pattern for $SrAl_2O_4$ [34].

3.2. Photoluminescence Properties. While undoped strontium aluminate nanosized particles (**1**) do not show any luminescence, Eu^{2+}-doped $SrAl_2O_4$ nanosized particles (**2–4**) show an identical spectroscopic behaviour at room temperature. For this reason, the luminescence spectra at room temperature are explained in this work in a general way, based, for example, on the measurements carried out on compound **4**. Immediately after combustion, the NP precursors contain a mixture of trivalent and divalent europium, due to the partial reduction caused by the urea and the generated reductive gases (Figure 4(a)). The inset suggests that the sample is simultaneously doped by Eu^{2+} (green emission) and Eu^{3+} (red emission). The mixed valence of europium is also indicated by the emission spectrum, where the broad band centered at 19 310 cm^{-1} (518 nm) is assigned in the literature to the $4f^6 5d^1 \rightarrow 4f^7$ ($^8S_{7/2}$) transition of Eu^{2+} and the shoulder at 16 260 cm^{-1} (615 nm) corresponds to the $^5D_0 \rightarrow {}^7F_2$ transition of Eu^{3+} (Figure 4(b)).

After sintering under an Ar/H_2 atmosphere, the remaining Eu^{3+} ions are completely reduced to Eu^{2+} exhibiting a homogeneous very intense green emission upon irradiation of UV light (Figure 5(a)). The respective emission and excitation spectra are depicted in Figure 5(b) and (c). Luminescence properties of $SrAl_2O_4$:Eu^{2+} nanoparticles have been intensively discussed in the literature [24, 27–32]. In the emission spectrum at room temperature only one broad band is observed located at 19 230 cm^{-1} (520 nm) with a full width at half maximum (FWHM) of 3 030 cm^{-1}. We will address the origin of this band in Figure 5.

At lower temperature, for example, 10 K, however, the presence of a second emission band (Figure 6(a), $\tilde{\nu}_{ex}$ = 27 620 cm^{-1}) located at 22 470 cm^{-1} (445 nm) is noted for

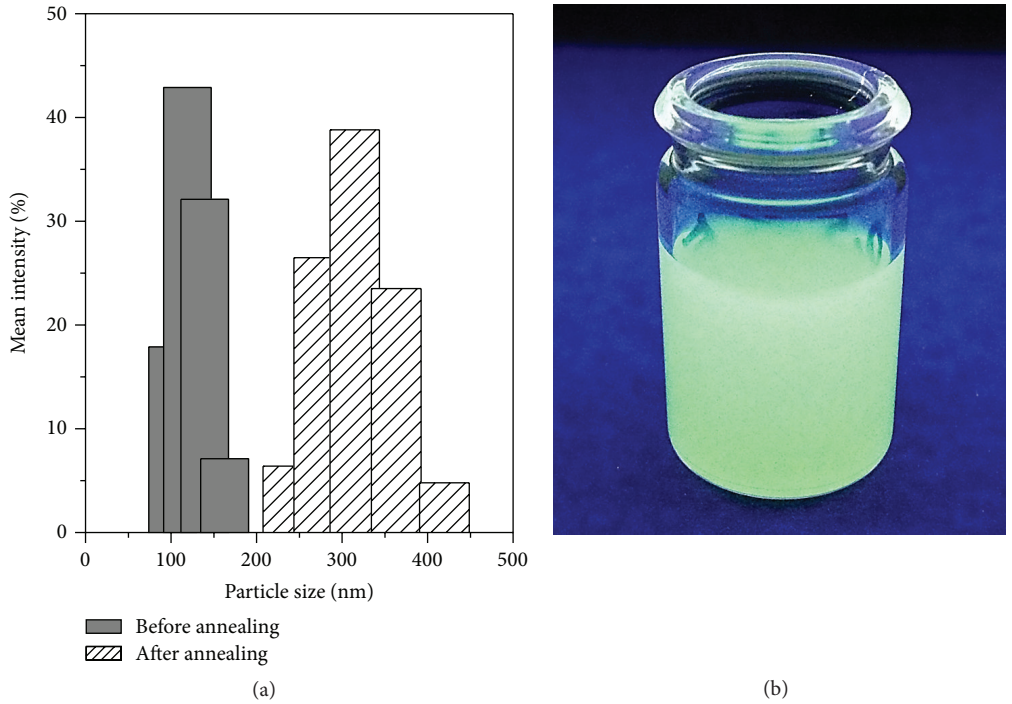

FIGURE 2: (a) Particle size distribution of $SrAl_2O_4$:Eu NPs, before and after annealing. (b) Ethanolic suspension of $SrAl_2O_4$:Eu^{2+} NPs under UV light.

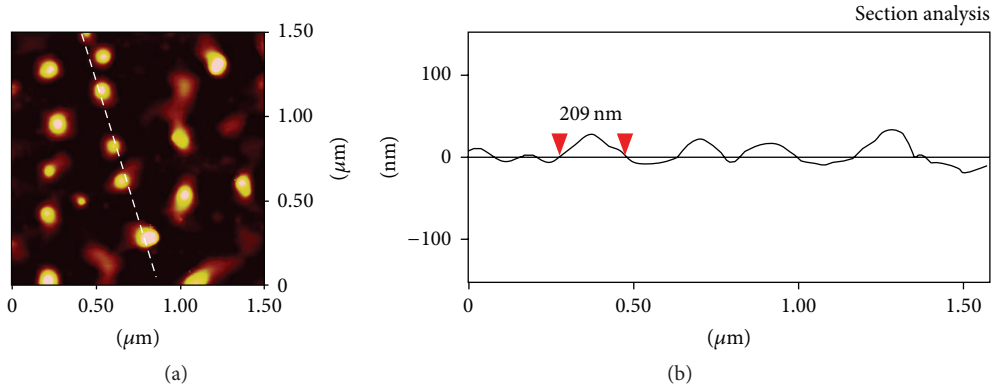

FIGURE 3: Atomic force microscope images of $SrAl_2O_4$:Eu^{2+} (a) and respective cross section analysis (b).

compounds **2**–**5**, in agreement with various reports from literature [35]. Its presence is, however, still intensively debated up to now. The excitation spectrum measured for the blue band of the $SrAl_2O_4$:Eu^{2+} nanosized phosphor consists of two broad bands. One of the bands covers a range between 24500 and 30000 cm^{-1} whereas the other structureless band is found at 35 470 cm^{-1} (Figure 6(b), $\tilde{\upsilon}_{em}$ = 22 520 cm^{-1}). Considering the crystal structure of $SrAl_2O_4$, there are two different Sr^{2+} sites, which are surrounded by six oxygen ions. They provide distorted octahedral site symmetry for the Eu^{2+} ions. The distortion from O_h symmetry can be, however, neglected to a first approximation. Therefore, it is possible to identify the two broad bands in the excitation spectrum (Figure 6(b)) with the 4f-5d transitions into the t_{2g} and e_g state, respectively, at a first approximation. The observed energy difference of roughly 8 520 cm^{-1} between the two bands in the excitation spectrum lies in the energy range predicted by DFT calculations of the density of the $4f^6$5d states of Eu^{2+} in $SrAl_2O_4$:Eu^{2+} by Hölsä et al. [14], which makes such an assignment initially plausible. It can therefore be interpreted as the crystal field splitting 10 *Dq* between the t_{2g} and the e_g state of the Eu^{2+} ions occupying the Sr^{2+} sites, as depicted in Figure 6(b).

Recording the excitation spectrum at 10 K for the blue emission band at 22 520 cm^{-1}, it is even possible to observe a raw fine structure in the excitation band assigned to the 4f-5d transition into the t_{2g} state. It can be well explained by the presence of the $4f^6$ core in the excited state that gives rise to

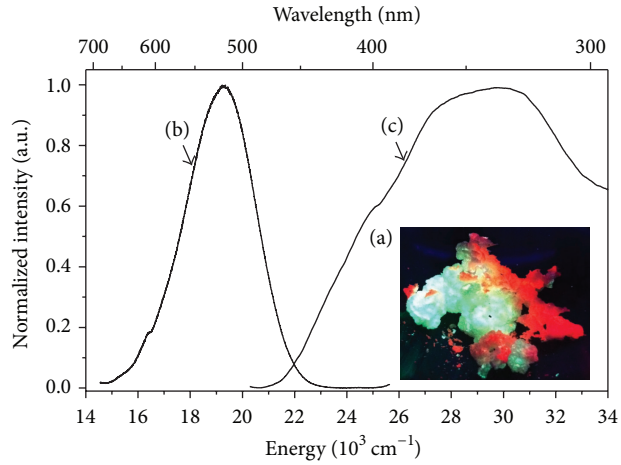

FIGURE 4: (a) Precursor of **4** irradiated with UV light. (b) Emission ($\tilde{\nu}_{ex}$ = 27 400 cm^{-1}) and (c) excitation ($\tilde{\nu}_{em}$ = 19 310 cm^{-1}) spectra of **4** after combustion synthesis.

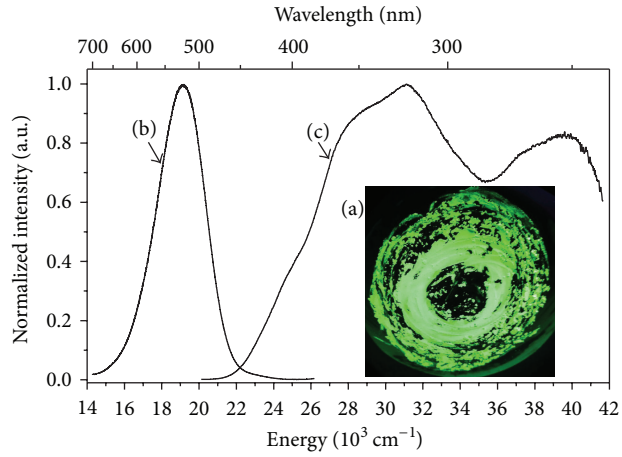

FIGURE 5: (a) **4** after annealing under reductive atmosphere, irradiated with UV light. (b) Emission ($\tilde{\nu}_{ex}$ = 27 624 cm^{-1}) and (c) excitation ($\tilde{\nu}_{em}$ = 19 417 cm^{-1}) spectra of reduced **4** at room temperature.

the different ^7F_J (J = 0–6) states by Coulomb repulsion and spin-orbit coupling. Their energies are compiled in Table 2 and their positions relative to the $^7F_0$ state are in good agreement with the values known from Eu^{3+} [15]. This already indicates a weak exchange coupling between the 4f electrons and the 5d electron in the excited state [16]. The lower resolution of this fine structure even at 10 K can be explained by the presence of two Sr^{2+} sites and the resulting overlap of the respective excitation spectra that should be similar in energy and appearance. Moreover, this fine structure is in general much better resolved in halide than in oxide host lattices due to the weaker coupling of 4f and 5d electrons, as it is nicely illustrated for $CsMBr_3$:Eu^{2+} (M = Mg, Ca, Sr) [36].

The knowledge about the positions of the ^7F_J states allows a relatively precise determination of the Stokes shift for Eu^{2+}

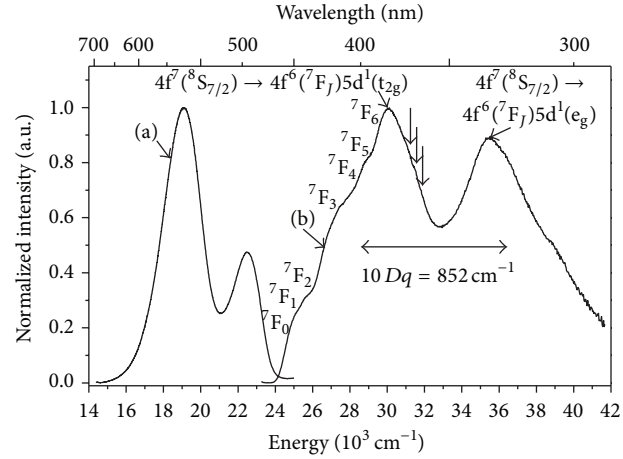

FIGURE 6: Emission ($\tilde{\nu}_{ex}$ = 27 620 cm^{-1}) and (b) excitation ($\tilde{\nu}_{em}$ = 22 520 cm^{-1}) spectra of **5** recorded at 10 K. The positions marked with arrows indicate Fano antiresonances due to $^8S_{7/2} \rightarrow {}^6I_J$ transitions.

TABLE 2: Energetic positions of the ^7F_J states in the t_{2g} excitation band in compound **5** and energy differences relative to the $^7F_0$ state.

State ^7F_J	Position/cm^{-1}	ΔE_{J-0}/cm^{-1}
$^7F_0$	24500	0
$^7F_1$	25010	510
$^7F_2$	25710	1210
$^7F_3$	26640	2140
$^7F_4$	27770	3270
$^7F_5$	28960	4460
$^7F_6$	30040	5540

TABLE 3: Energetic positions of the Fano antiresonances in $SrAl_2O_4$:Eu^{2+}.

State ^6I_J	Position/cm^{-1}
$^6I_{7/2}$	31 350
$^6I_{9/2}$	31 650

in this compound, namely, ΔE_s = 1 980 cm^{-1}. This is in good agreement with the values typically known from Eu^{2+} [3].

In the region of 31000–32000 cm^{-1}, two little dips are observable (see Table 3), as marked by arrows in Figure 6(b) and shown in Figure 7 more illustratively. Their positions coincide with the energies of $^8S_{7/2} \rightarrow {}^6I_J$ (J = 7/2, 9/2) transitions within the $4f^7$ configuration of Eu^{2+} [37]. Since the nature of 4f-4f transitions makes their energies nearly independent of the host compound, their presence allows an undoubted interpretation. Thus, these dips can be assigned to Fano antiresonances [38] between the $^8S_{7/2} \rightarrow {}^6I_J$ transitions and the 4f-5d transition of Eu^{2+}. There exist some examples in literature in which this phenomenon has already been observed such as Eu^{2+}-activated haloborates $M_2B_5O_9X$ (M = Sr, Ba; X = Cl, Br) [39] or $Sr(SCN)_2$:Eu^{2+} [40]. The positions of the Fano antiresonances reported thereof coincide nicely with our values justifying this assignment. The presence of

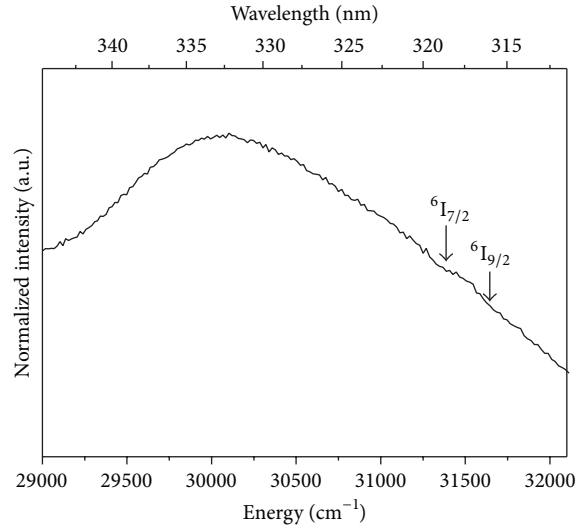

FIGURE 7: Fano antiresonances in the excitation spectrum of 5 ($\tilde{\nu}_{em}$ = 22 520 cm^{-1}) recorded at 10 K.

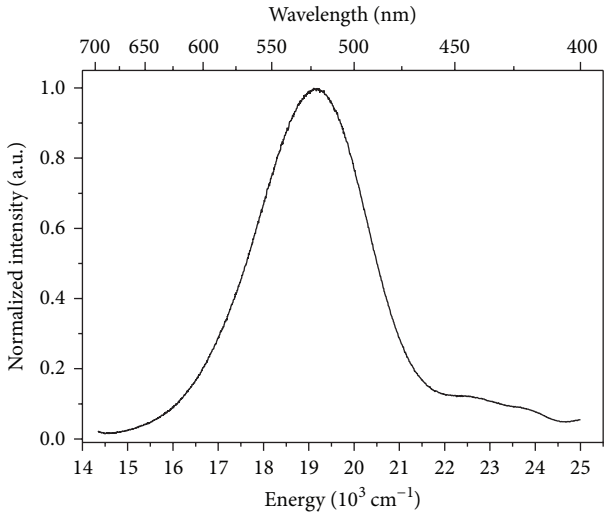

FIGURE 8: Emission spectrum of **5** ($\tilde{\nu}_{ex}$ = 27 620 cm^{-1}) recorded at 250 K.

the Fano antiresonances additionally confirms the interpretation of the blue emission at 22 520 cm^{-1} as a 5d-4f emission of Eu^{2+}.

Another hint on this assignment of the bands given above is the luminescence of $CaAl_2O_4$:Eu^{2+} with a blue emission at 22 900 cm^{-1} (437 nm) [41]. However, the unexpected slight blueshift compared to $SrAl_2O_4$ could be explained by the different coordination spheres in both compounds due to different crystal structures [34, 42]. The occupation of two Sr^{2+} sites by Eu^{2+} is nicely confirmed in the emission spectrum (Figure 8) at temperatures lower than room temperatures, in which actually two blue emissions are rawly resolved at about 22 750 cm^{-1} (440 nm) and 23 920 cm^{-1} (418 nm). This is a strong evidence that our assignment is plausible.

Considering once more the emission and excitation spectrum of sample **4** recorded at room temperature (Figure 5), a green emission at 19 230 cm^{-1} (520 nm) is observed that is also detected at 10 K. The slight asymmetry can be attributed to the presence of two Sr sites leading to a convoluted signal in the emission. For the excitation spectrum obtained upon detection of this emission (Figure 5(c)), a certain similarity to the respective excitation spectrum of the blue emission is noted (s. Figure 6(b)) although the former is spread over a larger part and contains a less well-defined fine structure. This can be partly attributed to the effect of vibrational broadening at room temperature. Since the appearance of this excitation spectrum does not change significantly at 10 K, this cannot be the only reason. In fact, the large FWHM of the emission of 3 030 cm^{-1} at room temperature and the large Stokes shift of roughly 5 270 cm^{-1} taking the position of the $4f^6(^7F_0)5d(t_{2g})$ state as reference already indicate an anomalous behavior of this luminescence [43]. The close location of the 5d states of Eu^{2+} to the conduction band in $SrAl_2O_4$ is already well-known [44]. Therefore, we also imply that the green emission involves delocalization of the excited electron into the conduction band thus leading to the formation of an impurity-trapped exciton at Eu^{2+} [43]. An involvement of the conduction band states seems very probable from luminescence decay measurements of the blue emission band [35]. A relatively small decay time of 0.42 μs was reported for this emission, compared to other Eu^{2+}-activated compounds; this lifetime is rather short [45]. Moreover, the decay is not monoexponential indicating interactions with the host compound. Both observations strongly favor this interpretation giving rise to an anomalous luminescence of Eu^{2+}.

The fact that both bands arise from the presence of Eu^{2+} ions in the host compound is illustrated in Figure 9. It shows the emission spectra recorded at 10 K of strontium aluminate nanosized particles with different europium concentrations. The $SrAl_2O_4$ nanosized particles without europium do not show any luminescence whereas, for the ones with Eu^{2+}, the intensity at 22 520 cm^{-1} relative to the main emission peak at 19 230 cm^{-1} decreases with increasing Eu^{2+} concentration. These results had also been found by Clabau et al. [17]. They were interpreted in terms of an energy transfer from an assigned defect-correlated transition at 444 nm (22 520 cm^{-1}) to the Eu^{2+} ions emitting at 525 nm (19 230 cm^{-1}) [17, 35]. This makes sense in so far since the higher-energy emission slightly overlaps with the excitation spectrum related to the Eu^{2+} emission (see Figures 4 and 5), which is a necessary condition for a resonant energy transfer. As we have shown above, however, the blue emission band at 444 nm (22 520 cm^{-1}) arises from Eu^{2+} itself. Our interpretation of the result is rather that a higher Eu^{2+} concentration induces a 5d band formation rather than the presence of localized states within the band gap. This band formation reduces the thermal activation barrier for the 5d electron to become delocalized into the conduction band. Therefore, the intensity of the blue emission should decrease with increasing Eu^{2+} concentration, as it is observed.

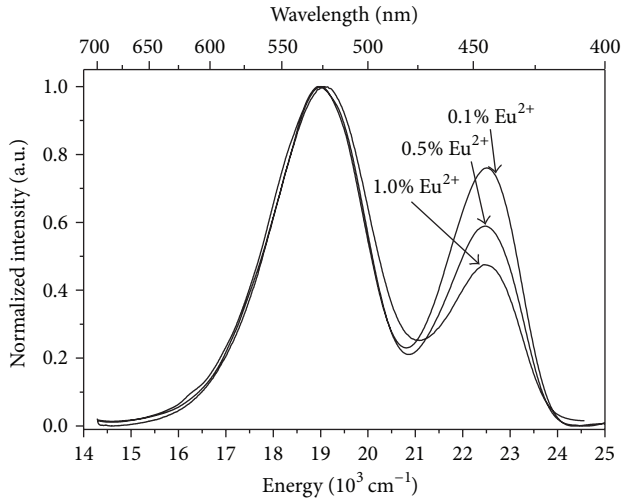

FIGURE 9: Emission spectra ($\bar{\upsilon}_{ex}$ = 27 620 cm^{-1}) of **2** (0.1% Eu^{2+}), **3** (0.5% Eu^{2+}), and **5** (1.0% Eu^{2+}) at 10 K.

The luminescence spectra of $SrAl_2O_4$:Eu^{2+} (**2**–**4**) and $SrAl_2O_4$:Eu^{2+},Dy^{3+} (**5**) are identical, and the latter are therefore not separately discussed here. Interestingly, no 4f-4f transitions from Dy^{3+} are detected. However, the addition of Dy^{3+} is responsible for the generation of an additional afterglow effect, which lasts for at least 42 minutes noticeably (Figure 10).

There exist various mechanisms in literature regarding how the relaxation processes in the excited state occur resulting in the green emission as well as the afterglow. Several interpretations were attempted, as indicated above [12, 15, 35]. A good overview can be found in the work of Clabau et al. [17]. In fact, up to now, their suggested mechanism for the afterglow seems to be the most reasonable one although our interpretation of the blue emission band as a 5d-4f transition due to Eu^{2+} differs from their assignment due to a charge-transfer-type transition from the valence band to residual Eu^{3+} ions [17]. The presence of residual Eu^{3+} ions is one of the key assumptions of the afterglow mechanism from Clabau et al. [17]. In fact, it was recently shown by XANES measurements that this assumption is valid [46]. Due to the well-resolved fine structure in the excitation spectrum (see Figure 6(b)) and the fact that such a CT-like transition would be accompanied by an enormous Stokes shift, we think that the assignment to normal Eu^{2+} luminescence is legitimate. More investigations are required in order to clarify all details of the mechanism for the afterglow and its dependence upon the type of trivalent impurity unambiguously.

Moreover, heating up the sample from 10 K to room temperature (Figure 11), a gradual decrease of the overall emission intensity is observed. This behaviour is expected due to the loss of energy by means of nonradiative transitions at higher temperatures. In order to gain an insight into the thermal activation of the 5d electrons into the conduction band, the integrated intensities of the blue emission band at 22 520 cm^{-1} were investigated dependent upon the temperature, as depicted in Figure 12. The integrated emission intensities are normalized to the value at 10 K. In this diagram, the integrated emission intensity of **5** at 22 520 cm^{-1} decreases by almost 100%, when heated from 10 K up to room temperature. The decay of the intensity signal can be fitted to the Mott equation:

$$\frac{I(T)}{I_0} = \frac{1}{1 + c \cdot \exp\left(-E_a/k_B T\right)}, \quad (1)$$

where $c = p/k_{rad}$ is the ratio between the thermal quenching rate and the rate for the radiative decay and E_a is the activation barrier for the nonradiative process.

From the fit to (3), an activation barrier for the thermal quenching of (455 ± 95) cm^{-1} is obtained. The low value for the reduced χ^2 value indicates a reasonable description of the points by (3) taking into account that there are only seven data points and two free parameters. The adjusted R^2 value is also acceptable. Within the error, the activation energy lies in the range of the phonon energy of $SrAl_2O_4$, as indicated by the Raman measurements presented in Figure 14. Thus, it seems reasonable that the thermal activation to the conduction band is mediated via electron-phonon coupling to the lattice phonons of the host compound $SrAl_2O_4$. Moreover, the value (56 meV) is larger than the reported threshold requiring exciting the 5d electron into the conduction band (17 meV) [7, 47]. This indicates that one phonon is already sufficient to overcome this barrier. Out of the data, the quenching temperature $T_{1/2}$, at which 50% of the initial intensity is still observed, can be deduced to be roughly 160 K.

In order to further investigate the effect of the temperature on the emission intensity, which is a very important measurement in the context of application in lamps, compound **5** was additionally heated. As shown in Figure 12, the emission intensity gradually decreases between 300 K and 500 K, and the emission is nearly fully quenched at 500 K. The large energy loss caused by nonradiative transitions is commonly observed for phosphors at high temperature and represents an obstacle for the application of $SrAl_2O_4$ for LED technology.

3.3. Electron-Phonon Coupling Analysis of Doped $SrAl_2O_4$ NPs. A qualitative picture of the experimentally observed peculiarities in $SrAl_2O_4$:Eu^{2+} phosphors can be achieved in the framework of the model that includes linear vibronic interaction with a local vibration and with low frequency crystal modes [19]. Three main parameters describe the electron-vibrational interaction between the impurity ion and its surroundings: the Stokes shift ΔE_S (the difference in energy between the first absorption and emission peaks), the Pekar-Huang-Rhys factor S (which is proportional to ΔE_S), and the effective phonon energy $\hbar\omega$. Since the band exhibits a distinct vibronic structure it is worthwhile to assume that the main contribution to the width and to the Stokes shift is provided by the local vibration while the electron-phonon interaction is relatively weak playing the role of a smoothening factor. Neglecting this contribution that is assumed to be small one can express the full Stokes

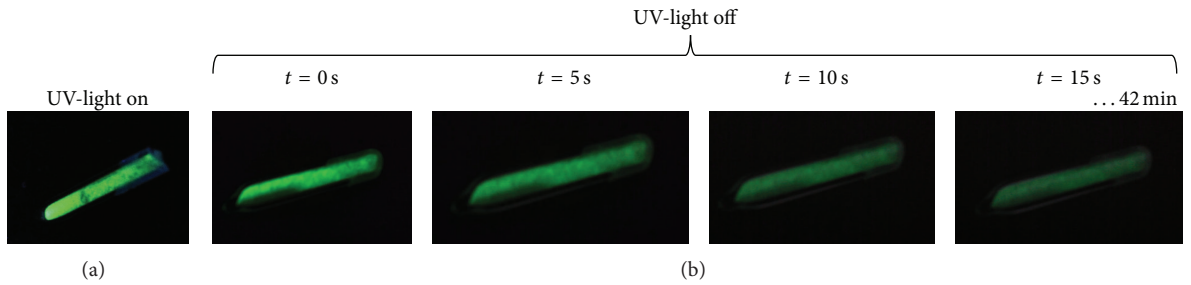

FIGURE 10: Green luminescence of **5** under UV light (left) and afterglow effect with duration up to 42 minutes after turning the UV light off (right).

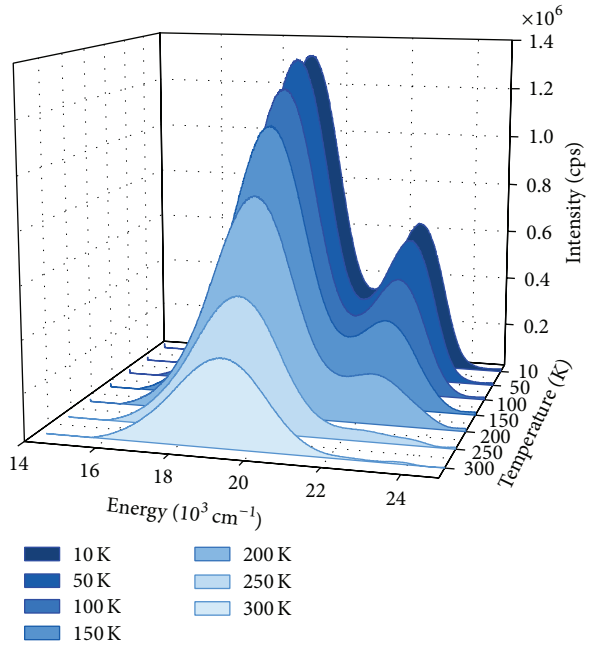

FIGURE 11: Effect of decreased temperatures on the emission spectrum ($\tilde{\upsilon}_{ex}$ = 27 620 cm^{-1}) of **5**.

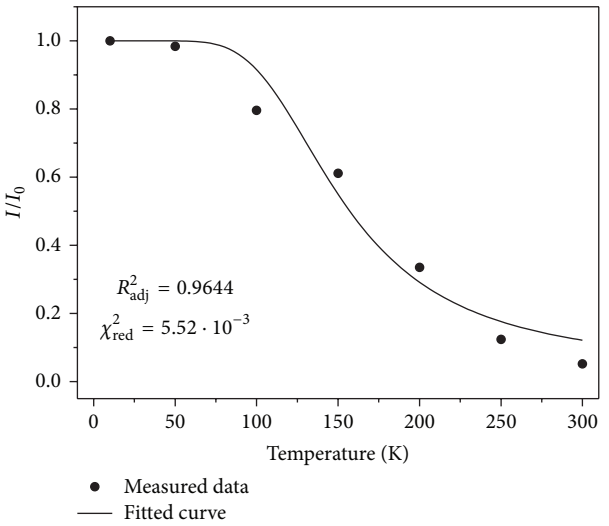

FIGURE 12: Decrease of the integrated emission intensity at 22 470 cm^{-1} ($\tilde{\upsilon}_{ex}$ = 27 620 cm^{-1}) of **5** with increasing temperature. The solid line is a fit to (3).

shift through the Pekar-Huang-Rhys factor S related to the local vibration as

$$\Delta E_S = (2S - 1)\,\hbar\omega. \tag{2}$$

The temperature variation of the half-width (full width at half maximum, FWHM) can be expressed as

$$\text{FWHM}\,(T) = 2.35 \cdot \sqrt{S} \cdot \hbar\omega \cdot \coth\left(\frac{\hbar\omega}{2k_BT}\right). \tag{3}$$

These expressions can be employed for the estimation of the Pekar-Huang-Rhys factor and average phonon energy $\hbar\omega$. Taking the position of the $4f^6(^7F_0)5d^1(t_{2g})$ excitation band at 24 500 cm^{-1} (see Table 2), the green emission band maximum at 19 230 cm^{-1} (Figure 5), and FWHM of the emission band as 3 030 cm^{-1} at 300 K, (2) and (3) yield the following values of the Stokes shift, Pekar-Huang-Rhys factor, and effective phonon energy: ΔE_S = 5270 cm^{-1}, S = 6, and $\hbar\omega$ = 480 cm^{-1}. It is also possible to analyse the linear vibronic interaction of the blue Eu^{2+} emission band at 22 520 cm^{-1}. For that, we have used the convoluted FWHM at 10 K of 1 840 cm^{-1}. With ΔE_S = 1 980 cm^{-1}, a Pekar-Huang-Rhys factor of S = 2.5 and an average phonon energy of $\hbar\omega$ = 470 cm^{-1} are obtained. Both phonon energies are in very good agreement with the value deduced from the thermal quenching analysis as shown in Figure 11 for the blue emission as well as from the Raman measurements (see Figure 13). This again indicates a deep correlation between the green and the blue emission in $SrAl_2O_4$. Very similar values have already been reported by Nazarov et al. [19]. It has to be taken into account, however, that the underlying model does not include the presence of two Sr^{2+} sites as well as the participation of the conduction band. Therefore, these values should be considered as estimations rather than exact values.

A similar consideration of the electron-vibrational interaction for Eu^{2+} in $SrGa_2S_4$, $CaGa_2S_4$, and $BaGa_2S_4$ doped with Eu^{2+} was published recently [20–22] with the values of S from 4 to 7 and phonon energies around 300 cm^{-1}. A higher

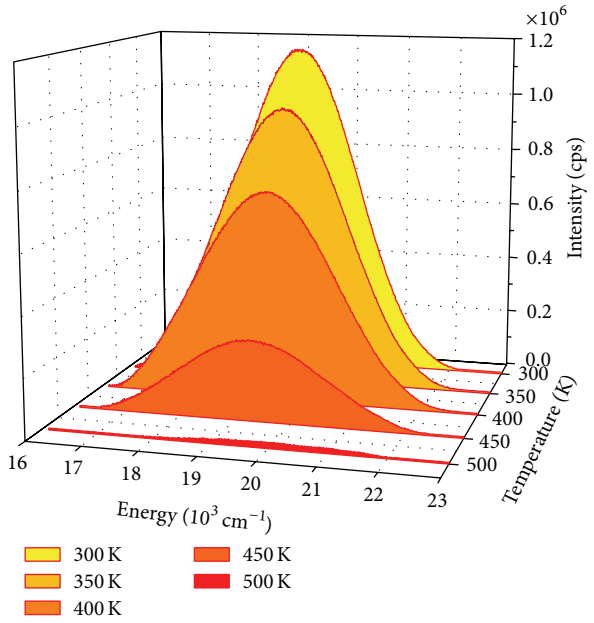

Figure 13: Effect of increased temperatures on the emission spectrum ($\bar{\upsilon}_{ex}$ = 27 620 cm^{-1}) of **5** NPs.

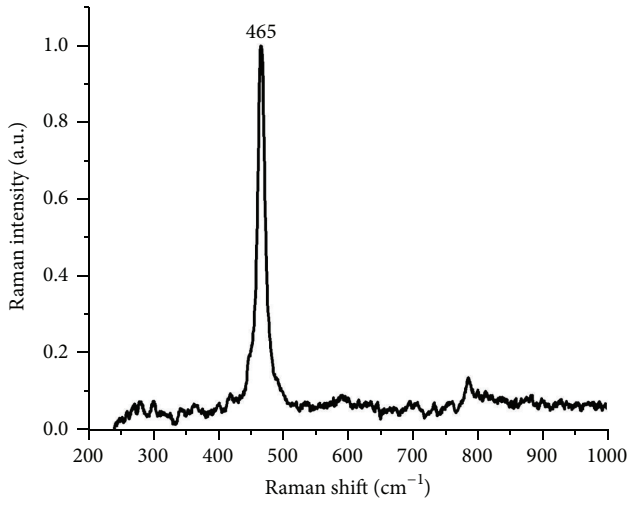

Figure 14: Results of Raman spectroscopy for $SrAl_2O_4$ NPs excited at 514 nm laser wavelength.

value of the Pekar-Huang-Rhys factor in our analysis can be readily explained by a large Stokes shift (about 5 200 cm^{-1}).

In order to enhance the understanding of the doping effect from the structural point of view, Raman scattering study is a very useful tool for investigating the lattice vibrational modes, which can provide details of lattice vibration changes. Due to the monoclinic symmetry of the compound, no mutual exclusion of vibrational modes occurs such that IR spectroscopy would afford the same results and was thus left out. Raman measurements were repeated several times, under the conditions described in the experimental part, from different points of the sample and registered the same

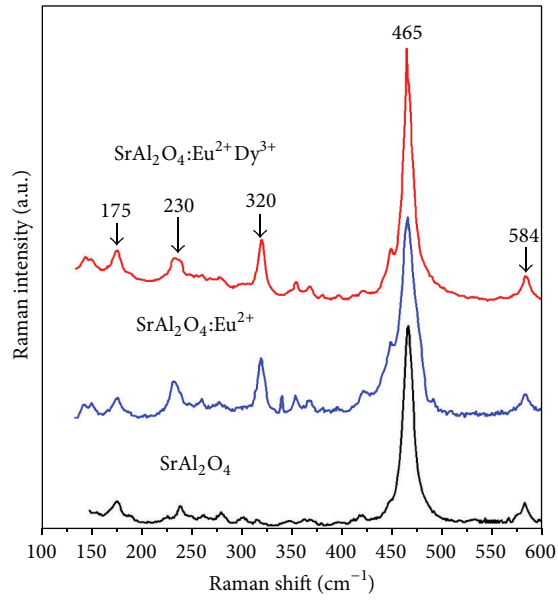

Figure 15: Results of Raman spectroscopy for $SrAl_2O_4$ NPs undoped (black curve), doped with Eu^{2+} (blue curve), and codoped with Eu^{2+} and Dy^{3+}, under excitation by 633 nm laser wavelength.

spectra as shown in Figure 13, which confirms the homogeneity of the prepared materials. To a first approximation, we attribute modes at a frequency higher than 600 cm^{-1} to Al–O stretching vibrations and the narrow low-frequency peaks below 250 cm^{-1} (not shown in Figure 13) to tetrahedral vibrations or tilts. In the intermediate region, the assignment is impossible. By analogy with other compounds, we assign the most intense band at 465 cm^{-1} to the bending vibration of the O–Al–O group within the $[AlO_4]^{5-}$ tetrahedra [48]. Obviously, it is this vibration that is coupled to for the electron-phonon interactions.

This intermediate part of the spectra is the most important one and this region (100–600 cm^{-1}) was measured carefully for all samples and shown in Figure 15. The profiles (a, b, c) correspond to the Raman spectra of the $SrAl_2O_4$, $SrAl_2O_4$:Eu^{2+} and $SrAl_2O_4$:Eu^{2+}, Dy^{3+} compositions, respectively. Theoretically, the Raman selection rules allow 81 active modes for monoclinic $SrAl_2O_4$ doped with Eu^{2+} [49]. However, as shown in Figure 15, in the Raman spectra of Eu^{2+}- and Dy^{3+}-doped $SrAl_2O_4$, less than 14 active modes were observed, which is partially due to the possible overlap of some symmetry vibrations or the weak features of some Raman bands [50]. All spectra exhibit a strong peak at 465 cm^{-1} attributed to the bending of O–Al–O bonds in the corner-sharing tetrahedral. This indicates that the samples present very closely monoclinic structures. The Raman spectra of $SrAl_2O_4$:Eu^{2+} and $SrAl_2O_4$:Eu^{2+}, Dy^{3+} are similar to the host $SrAl_2O_4$; however, they show several differences: a second peak evolves at 450 cm^{-1} with higher dopant concentration. According to our assignment above, this can be interpreted as a distortion of the $[AlO_4]^{5-}$ tetrahedra and the crystal structure due to the doping. Moreover, other peaks at

230 and 320 cm^{-1} become stronger, and the width of strongest mode at 465 cm^{-1} has increased for doped phosphors. The presence of further local modes of the $[EuO_n]$ and $[DyO_m]$ polyhedra, respectively, can be probably neglected here due to the very low concentration of the dopant ions such that the presence of these peaks can be probably also correlated with a descent in symmetry because of doping.

3.4. $SrAl_2O_4:Eu^{2+}$-Based LED Coat. In phosphor conversion white LEDs, noble phosphor materials play a crucial role in high quality white emission. In contradiction to the analogous bulk samples, luminescent NPs present several advantages such as high packing density, low light scattering effects, and energy saving synthesis (with shorter preparation time and lower sintering temperatures) and are easily suspendable in liquid media. Due to the small size, NPs are able to build thinner films, for example, on the surface of LEDs, and are less subjected to concentration quenching effects when compared to doped micron-sized phosphors. For LED applications, prepared NPs were combined with InGaAlN-based UV LED chip (chip size (400 ± 25) μm × (400 ± 25) μm, thickness (80 ± 10) μm) as an optical pumping source, and the performances of fabricated LEDs were investigated. Phosphor conversion LEDs were fabricated by combining UV LED as an optical pumping source with post-heat-treated $SrAl_2O_4:Eu^{2+}$ NPs. The NPs were mixed with transparent silicone gel (1 : 10 wt%) and coated onto the lead frame with UV chip with maximum emission at about 350 nm. Figure 16 shows the emission spectrum (Lab Sphere) of the fabricated LEDs.

The $SrAl_2O_4:Eu^{2+}$ NPs were excited by UV light and generated green emission. The CIE-1931 coordinates of $SrAl_2O_4:Eu^{2+}$ phosphors conversion LEDs were in the green region at 20 mA (x = 0.288 and y = 0.547, Figure 16). The excitation intensity and corresponding emission peak showed that the $SrAl_2O_4:Eu^{2+}$ was suitable green phosphor for UV excited white LEDs.

4. Conclusions

In this work, strontium aluminate nanoparticles were prepared by means of combustion synthesis. The particles were produced with different Eu^{2+} concentrations (**2**–**4**) as well as undoped (**1**) and codoped with Dy^{3+} (**5**) with the objective of elucidating open questions concerning the luminescence on $SrAl_2O_4:Eu^{2+}$, Dy^{3+}. Dynamic light scattering revealed an increase of the particle size after the postsynthetic annealing step and the formation of small particle agglomerates. Measurements of single particles were carried out with aid of cross section AFM analysis, resulting in the estimation of the particle size in 200–300 nm. Due to the small size, the particles were able to form stable suspensions in liquid media, which show very bright green luminescence under UV light.

After combustion, a voluminous precursor is formed, whose emission spectrum at room temperature is characterized by a strong green emission at 19 230 cm^{-1} (520 nm) assigned in the literature to Eu^{2+} and a shoulder at 16 260 cm^{-1} (615 nm) that corresponds to the $^5D_0 \rightarrow {}^7F_2$ transition of Eu^{3+}. After annealing under reducing atmosphere, only Eu^{2+} ions are present. At low temperatures, an additional band emerges at 22 520 cm^{-1} (444 nm). The well-resolved fine structure in the excitation spectra excitation ($\tilde{\nu}_{em}$ = 22 520 cm^{-1}) due to the different ^7F_J states of the $4f^6$ core in the excited state as well as the presence of Fano antiresonances with the ^6I_J states made the assignment of the emission band at 22 520 cm^{-1} to the $4f^6(^7F_J)5d^1(t_{2g}) \rightarrow 4f^7(^8S_{7/2})$ transition of Eu^{2+} occupying both Sr^{2+} sites in $SrAl_2O_4$ plausible. The coordination can be assumed to be octahedral for both Sr^{2+} sites to a first approximation, leading to a crystal field splitting of 10 Dq = 8520 cm^{-1}, as is predicted by DFT calculations [14]. Moreover, at temperatures lower than 250 K, the emission bands of Eu^{2+} on both Sr^{2+} sites can be resolved into two emission bands centered at 22 750 cm^{-1} and 23 920 cm^{-1}, also confirming our assignment. Based on that interpretation, we assigned the green emission to a rather anomalous luminescence of Eu^{2+} arising upon thermal activation of the 5d electron into the conduction band and subsequent relaxation as indicated by the low quenching temperature of 160 K. The presence of Dy^{3+} leads to an efficient afterglow of the green emission. The details of the evolvement of the green emission and the afterglow, however, still have to be elucidated. Both the thermal quenching analysis and the calculation of the average phonon energy and the Huang-Rhys parameters S indicate the coupling to the $[AlO_4]^{5-}$ bending modes. The calculated energies fit nicely with the value observed in Raman measurements. By that, we attempted to show that the green emission is deeply correlated to the presence of the blue emission. Finally, it could be illustrated that the produced $SrAl_2O_4:Eu^{2+}$-based LED coat shows efficient green luminescence that might be interesting for applications in lighting technology.

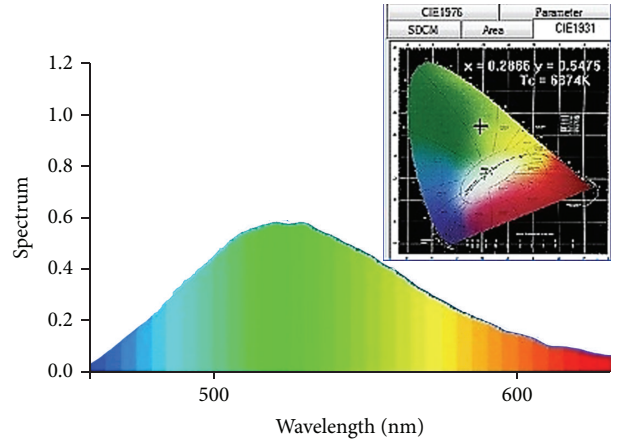

Figure 16: Emission spectrum and CIE-1931 coordinates of fabricated LED.

Conflict of Interests

The authors declare that there is no conflict of interests regarding the publication of this paper.

Acknowledgments

The authors thank Peter Krolla-Sidenstein for the assistance during the AFM measurements and Professor Dr. Christof Wöll, KIT Karlsruhe, Germany, for using his equipment.

References

[1] Y. Zheng and D. Chen, "Luminescence studies on $Al_4B_2O_9$:Eu^{2+} phosphor crystals," *Luminescence*, vol. 26, no. 6, pp. 481–485, 2011.

[2] N. Salah, S. S. Habib, and Z. H. Khan, "Quantum effect on the energy levels of Eu^{2+} doped $K_2Ca_2(SO_4)_3$ nanoparticles," *Journal of Fluorescence*, vol. 20, no. 5, pp. 1009–1015, 2010.

[3] P. Dorenbos, "Energy of the first $4f^7 \rightarrow 4f^6 5d$ transition of Eu^{2+} in inorganic compounds," *Journal of Luminescence*, vol. 104, no. 4, pp. 239–260, 2003.

[4] T. R. N. Kutty, R. Jagannathan, and R. P. Rao, "Luminescence of Eu^{2+} in strontium aluminates prepared by the hydrothermal method," *Materials Research Bulletin*, vol. 25, no. 11, pp. 1355–1362, 1990.

[5] H. Lin, X. R. Liu, and E. Y. B. Pun, "Sensitized luminescence and energy transfer in Ce^{3+} and Eu^{2+} codoped calcium magnesium chlorosilicate," *Optical Materials*, vol. 18, no. 4, pp. 397–401, 2002.

[6] P. Zhang, M.-X. Xu, Z.-T. Zheng, B. Sun, and Y.-H. Zhang, "Microwave synthesis and characterization of new red long afterglow phosphor $Sr_3Al_2O_6$:Eu," *Transactions of Nonferrous Metals Society of China*, vol. 16, pp. s423–s425, 2006.

[7] T. Matsuzawa, Y. Aoki, N. Takeuchi, and Y. Murayama, "A new long phosphorescent phosphor with high brightness, $SrAl_2O_4$:Eu^{2+},Dy^{3+}," *Journal of the Electrochemical Society*, vol. 143, no. 8, pp. 2670–2673, 1996.

[8] B. Cheng, Z. Zhang, Z. Han, Y. Xiao, and S. Lei, "$SrAl_2O_4$:Eu^{2+},Dy^{3+} nanobelts: synthesis by combustion and properties of long-persistent phosphorescence," *Journal of Materials Research*, vol. 26, no. 17, pp. 2311–2315, 2011.

[9] X. Yang, G. Ning, W. Pan, and Y. Lin, "Preparation of $SrAl_2O_4$: Eu, Dy phosphor by nano-coating process and its optical properties," in *Proceedings of the 1st IEEE International Conference on Nano Micro Engineered and Molecular Systems*, pp. 896–899, Zhuhai, China, January 2006.

[10] F. Yoshimura, K. Nakamura, F. Wakai et al., "Preparation of long-afterglow colloidal solution of $Sr_2MgSi_2O_7$: Eu^{2+}, Dy^{3+} by laser ablation in liquid," *Applied Surface Science*, vol. 257, no. 6, pp. 2170–2175, 2011.

[11] P. Dorenbos, "Mechanism of persistent luminescence in Eu^{2+} and Dy^{3+} codoped aluminate and silicate compounds," *Journal of the Electrochemical Society*, vol. 152, no. 7, pp. H107–H110, 2005.

[12] J. Hölsä, H. Jungner, M. Lastusaari, and J. Niittykoski, "Persistent luminescence of Eu^{2+} doped alkaline earth aluminates, MAl_2O_4:Eu^{2+}," *Journal of Alloys and Compounds*, vol. 323-324, pp. 326–330, 2001.

[13] T. Aitasalo, J. Hölsä, H. Jungner, M. Lastusaari, and J. Niittykoski, "Mechanisms of persistent luminescence in Eu^{2+}, RE^{3+} doped alkaline earth aluminates," *Journal of Luminescence*, vol. 94-95, pp. 59–63, 2001.

[14] J. Hölsä, T. Laamanen, M. Lastusaari, M. Malkamäki, and P. Novák, "HASYLAB Annual Report," Tech. Rep., 2009.

[15] W. T. Carnall, G. L. Goodman, K. Rajnak, and R. S. Rana, "A systematic analysis of the spectra of the lanthanides doped into single crystal LaF_3," *The Journal of Chemical Physics*, vol. 90, no. 7, pp. 3443–3457, 1989.

[16] F. M. Ryan, W. Lehmann, D. W. Feldman, and J. Murphy, "Fine structure in the optical spectra of divalent europium in the alkaline earth sulfates," *Journal of the Electrochemical Society*, vol. 121, no. 11, pp. 1475–1481, 1974.

[17] F. Clabau, X. Rocquefelte, S. Jobic et al., "Mechanism of phosphorescence appropriate for the long-lasting phosphors Eu^{2+}-doped $SrAl_2O_4$ with codopants Dy^{3+} and B^{3+}," *Chemistry of Materials*, vol. 17, no. 15, pp. 3904–3912, 2005.

[18] M. Nazarov, A. Nor Nazida, S. C. M. Calyn, N. M. A. Aziz, and M. N. Ahmad-Fauzi, "Low-temperature luminescence of nanosized $SrAl_2O_4$:Eu^{2+}," *Moldavian Journal of the Physical Sciences*, vol. 11, no. 1-2, 2012.

[19] M. Nazarov, M. G. Brik, D. Spassky et al., "Phonon-assisted optical bands of nanosized powdery $SrAl_2O_4$:Eu^{2+} crystals: evidence of a multimode Pekarian," *Physics Letters A*, vol. 377, no. 43, pp. 3170–3178, 2013.

[20] M. Nazarov, B. Tsukerblat, and D. Y. Noh, "Electron-vibrational interaction in 4f-5d optical transitions in Ba, Ca, Sr thiogallates doped with Eu^{2+} ions," *Journal of Luminescence*, vol. 128, no. 9, pp. 1533–1540, 2008.

[21] M. Nazarov, B. Tsukerblat, and D. Y. Noh, "Vibronic coupling parameters and Stokes shift in thiogallate phosphors," *Journal of Physics and Chemistry of Solids*, vol. 69, no. 10, pp. 2605–2612, 2008.

[22] R. B. Jabbarov, C. Chartier, B. G. Tagiev et al., "Radiative properties of Eu^{2+} in $BaGa_2S_4$," *Journal of Physics and Chemistry of Solids*, vol. 66, no. 6, pp. 1049–1056, 2005.

[23] K. S. Bartwal, H. Ryu, M. G. Brik, and I. Sildos, "Preparation and spectroscopic studies of the $Mg_xSr_{1-x}Al_2O_4$:Eu, Dy ($x = 0.05 - 0.25$) persistent phosphors," *Optical Materials*, vol. 32, no. 10, pp. 1329–1332, 2010.

[24] T. Peng, H. Yang, X. Pu, B. Hu, Z. Jiang, and C. Yan, "Combustion synthesis and photoluminescence of $SrAl_2O_4$:Eu,Dy phosphor nanoparticles," *Materials Letters*, vol. 58, no. 3-4, pp. 352–356, 2004.

[25] H. C. Streit, J. Kramer, M. Suta, and C. Wickleder, "Red, Green, And blue photoluminescence of Ba_2siO_4: M (M = Eu^{3+}, Eu^{2+}, Sr^{2+}) nanophosphors," *Materials*, vol. 6, no. 8, pp. 3079–3093, 2013.

[26] S. S. Manoharan and K. C. Patil, "Combustion synthesis of metal chromite powders," *Journal of the American Ceramic Society*, vol. 75, no. 4, pp. 1012–1015, 1992.

[27] Z. Qiu, Y. Zhou, M. Lü, A. Zhang, and Q. Ma, "Combustion synthesis of long-persistent luminescent MAl_2O_4: Eu^{2+}, R^{3+} (M = Sr, Ba, Ca, R = Dy, Nd and La) nanoparticles and luminescence mechanism research," *Acta Materialia*, vol. 55, no. 8, pp. 2615–2620, 2007.

[28] R. Zhang, G. Han, L. Zhang, and B. Yang, "Gel combustion synthesis and luminescence properties of nanoparticles of monoclinic $SrAl_2O_4$:Eu^{2+},Dy^{3+}," *Materials Chemistry and Physics*, vol. 113, no. 1, pp. 255–259, 2009.

[29] P. Sharma, D. Haranath, H. Chander, and S. Singh, "Green chemistry-mediated synthesis of nanostructures of afterglow phosphor," *Applied Surface Science*, vol. 254, no. 13, pp. 4052–4055, 2008.

[30] N. M. Son, L. T. T. Vien, L. V. K. Bao, and N. N. Trac, "Synthesis of $SrAl_2O_4$:Eu^{2+} Dy^{3+} phosphorescence nanosized

powder by combustion method and its optical properties," *Journal of Physics: Conference Series*, vol. 187, no. 1, Article ID 012017, 2009.

[31] X. Yu, C. Zhou, X. He, Z. Peng, and S.-P. Yang, "The influence of some processing conditions on luminescence of $SrAl_2O_4:Eu^{2+}$ nanoparticles produced by combustion method," *Materials Letters*, vol. 58, no. 6, pp. 1087–1091, 2004.

[32] E. Shafia, M. Bodaghi, and M. Tahriri, "The influence of some processing conditions on host crystal structure and phosphorescence properties of $SrAl_2O_4:Eu^{2+}$, Dy^{3+} nanoparticle pigments synthesized by combustion technique," *Current Applied Physics*, vol. 10, no. 2, pp. 596–600, 2010.

[33] Z. Qi, C. Shi, M. Liu et al., "The valence of rare earth ions in $R_2MgSi_2O_7$: Eu, Dy (R = Ca, Sr) long-afterglow phosphors," *Physica Status Solidi A: Applied Research*, vol. 201, no. 14, pp. 3109–3112, 2004.

[34] A. R. Schulze and H. Müller-Buschbaum, "Compound formation $MeO:M_2O_3$. IV structure of monoclinic strontium aluminum oxide ($SrAl_2O_4$)," *Zeitschrift für Anorganische und Allgemeine Chemie*, vol. 475, pp. 205–210, 1981.

[35] T. Aitasalo, J. Hölsä, H. Jungner et al., "Effect of temperature on the luminescence processes of $SrAl_2O_4:Eu^{2+}$," *Radiation Measurements*, vol. 38, no. 4–6, pp. 727–730, 2004.

[36] M. Suta, P. Larsen, F. Lavoie-Cardinal, and C. Wickleder, "Photoluminescence of $CsMBr_3:Eu^{2+}$ (M=Mg, Ca, Sr)—a novel strategy for the development of low-energy emitting phosphors," *Journal of Luminescence*, vol. 149, pp. 35–44, 2014.

[37] J. Sugar and N. Spector, "Spectrum and energy levels of doubly ionized europium (Eu III)," *Journal of the Optical Society of America*, vol. 64, no. 11, pp. 1484–1497, 1974.

[38] U. Fano and J. W. Cooper, "Line profiles in the far-uv absorption spectra of the rare gases," *Physical Review A*, vol. 137, no. 5A, pp. A1364–A1379, 1965.

[39] A. Meijerink and G. Blasse, "Fano antiresonance in the excitation spectra of the luminescence of divalent europium," *Physical Review B: Condensed Matter and Materials Physics*, vol. 40, no. 10, pp. 7288–7291, 1989.

[40] C. Wickleder, "Thiocyanates as novel host lattices for emitting rare earth ions: luminescence of $Sr(SCN)_2:Eu^{2+}$," *Chemistry of Materials*, vol. 17, no. 5, pp. 1228–1233, 2005.

[41] C. E. Tyner and H. G. Drickamer, "Studies of luminescence efficiency of Eu^{2+} activated phosphors as a function of temperature and high pressure," *The Journal of Chemical Physics*, vol. 67, no. 9, pp. 4116–4123, 1977.

[42] W. Hörkner and H. Müller-Buschbaum, "Zur kristallstruktur von $CaAl_2O_4$," *Journal of Inorganic and Nuclear Chemistry*, vol. 38, no. 5, pp. 983–984, 1976.

[43] P. Dorenbos, "Anomalous luminescence of Eu^{2+} and Yb^{2+} in inorganic compounds," *Journal of Physics Condensed Matter*, vol. 15, no. 17, pp. 2645–2665, 2003.

[44] J. Ueda, T. Nakanishi, Y. Katayama, and S. Tanabe, "Optical and optoelectronic analysis of persistent luminescence in Eu^{2+}-Dy^{3+} codoped $SrAl_2O_4$ ceramic phosphor," *Physica Status Solidi C: Current Topics in Solid State Physics*, vol. 9, no. 12, pp. 2322–2325, 2012.

[45] S. H. M. Poort, A. Meijerink, and G. Blasse, "Lifetime measurements in Eu^{2+}-doped host lattices," *Journal of Physics and Chemistry of Solids*, vol. 58, no. 9, pp. 1451–1456, 1997.

[46] M. Lastusaari, H. F. Brito, S. Carlson et al., "Valences of dopants in Eu^{2+} persistent luminescence materials," *Physica Scripta*, vol. 89, no. 4, Article ID 044004, 2014.

[47] H. Yamamoto and T. Matsuzawa, "Mechanism of long phosphorescence of $SrAl_2O_4:Eu^{2+}$, Dy^{3+} and $CaAl_2O_4:Eu^{2+}$, Nd^{3+}," *Journal of Luminescence*, vol. 72–74, pp. 287–289, 1997.

[48] P. Escribano, M. Marchal, M. L. Sanjuán, P. Alonso-Gutiérrez, B. Julián, and E. Cordoncillo, "Low-temperature synthesis of $SrAl_2O_4$ by a modified sol-gel route: XRD and Raman characterization," *Journal of Solid State Chemistry*, vol. 178, no. 6, pp. 1978–1987, 2005.

[49] S. Hamdan, R. Hussin, M. A. Salim, M. S. Husin, D. N. F. Abdul Halim, and M. S. Abdullah, "Morphology and composition of strontium calcium aluminate matrix doped with Dy^{3+}," *Materials Science and Technology*, vol. 27, no. 1, pp. 232–234, 2011.

[50] K. Liang, Y. Qi, and C. Lu, "Temperature-dependent Raman scattering in ferroelectric $Bi_{4-x}Nd_xTi_3O_{12}$(x = 0, 0.5, 0.85) single crystals," *Journal of Raman Spectroscopy*, vol. 40, no. 12, pp. 2088–2091, 2009.